

Multiple-scattering lidar retrieval method: tests on Monte Carlo simulations and comparisons with *in situ* measurements

Luc R. Bissonnette, Gilles Roy, Laurent Poutier, Stewart G. Cober, and George A. Isaac

A multiple-field-of-view (MFOV) lidar measurement and solution technique has been developed to exploit the retrievable particle extinction and size information contained in the multiple-scattering contributions to aerosol lidar returns. We describe the proposed solution algorithm. The primary retrieved parameters are the extinction coefficient at the lidar wavelength and the effective particle diameter from which secondary products such as the extinction at other wavelengths and the liquid-water content (LWC) of liquid-phase clouds can be derived. The solutions are compared with true values in a series of Monte Carlo simulations and with in-cloud measurements. Good agreement is obtained for the simulations. For the field experiment, the retrieved effective droplet diameter and LWC for the available seven cases studied are on average 15% and 35% (worst case) smaller than the measured data, respectively. In the latter case, the analysis shows that the differences cannot be attributed solely to lidar inversion errors. Despite the limited penetration depth (150–300 m) of the lidar pulses, the results of the studied cases indicate that the retrieved lidar solutions remain statistically representative of measurements performed over the full cloud extent. Long-term MFOV lidar monitoring could thus become a practical and economical option for cloud statistical studies but more experimentation on more varied cloud conditions, especially for LWC, is still needed. © 2002 Optical Society of America

OCIS codes: 010.1310, 010.3640, 280.3640, 280.1310, 290.1090, 290.1310.

1. Introduction

To assess the effect of clouds on climate, it is necessary to characterize their microphysical and radiative properties. For low-level clouds, two parameters of primary concern are the liquid-water content (LWC) and the effective droplet diameter d_e . LWC is the liquid-water mass per unit volume of air and d_e is the ratio of the third-order to the second-order moments of the droplet size distribution.

The lidar or laser radar is an effective remote sen-

sor of clouds. The short visible to near-infrared wavelengths generally used for this application make the lidar particularly sensitive to small droplets. By comparison, millimeter-wave radar reflectivity is proportional to the sixth-order moment of the droplet size parameter $\pi d/\lambda$ and the lidar backscatter, to the second-order moment.¹ d is the droplet diameter and λ is the radar or lidar wavelength.

The lidar has been used extensively to map clouds at high spatial and temporal resolutions in programs such as the Experimental Cloud Lidar Pilot Study (ECLIPS), and to differentiate between solid-, liquid-, and mixed-phase clouds.² However, the quantitative retrieval of the optical extinction, and eventually LWC and d_e , has proved more elusive. General solutions^{3,4} exist for the extinction coefficient but there is the difficulty⁵ of having to specify a consistent boundary value, generally at the far end of the lidar range, and a backscatter-to-extinction ratio. The problem has been dealt with in many different ways. For example, there are limited cases that give rise to practical solution methods, for example, in optically thick⁶ and thin⁷ clouds. On the other hand, several techniques have been developed either to eliminate the need for a boundary value and backscatter-to-

L. R. Bissonnette (luc.bissonnette@drdc-rddc.gc) and G. Roy are with the Defence Research and Development Canada, 2459 Pie-XI Boulevard, North, Val-Bélair, Québec G3J 1X5, Canada. L. Poutier is with the Département d'Optique Théorique et Appliquée, Office National d'Études et Recherche Aéronautiques, Centre d'Études et de Recherches de Toulouse, 2 Avenue Edouard Belin, BP 4025, 31055 Toulouse Cedex 4, France. S. G. Cober and G. A. Isaac are with the Cloud Physics Research Division, Meteorological Service of Canada, 4905 Dufferin Street, Toronto, Ontario M3H 5T4, Canada.

Received 15 March 2002; revised manuscript received 14 June 2002.

0003-6935/02/306307-18\$15.00/0

© 2002 Optical Society of America

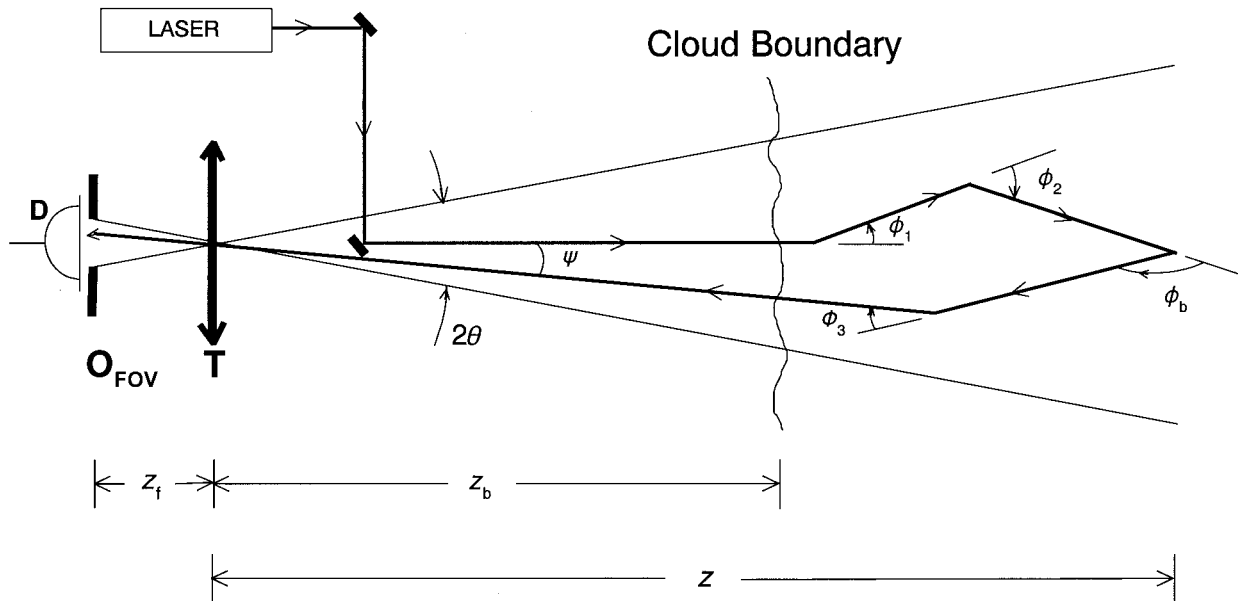


Fig. 1. Schematic of MFOV detection of multiply scattered lidar return: T, receiver telescope; z_f , focal distance; O_{FOV} , aperture defining receiver FOV; D, detector; z_b , range to cloud base; z , range to backscatter event; ϕ_i , forward-scattering angles; ϕ_b , backscattering angle; ψ , angle of collected photon; and θ , semiangle of receiver FOV. We achieved MFOV by varying O_{FOV} ; different approaches can be used.

extinction ratio as in the high spectral resolution^{8,9} and Raman¹⁰ lidar methods, or to reduce the arbitrariness by measurements^{11–13} and data processing.^{14–16} And the list is far from exhaustive.

In optically dense clouds, multiple scattering cannot be neglected. It constitutes an additional unknown defined, for example, by the parameter η in the Allen and Platt¹⁷ formalism. If neglected, it can seriously affect the precision of the retrieved quantities. Following the pioneering work of Allen and Platt,¹⁷ several groups have begun to model multiple scattering in lidar. A series of articles resulting from a coordinated simulation effort have been collected in a topical issue of *Applied Physics B*.¹⁸ From these and other studies it has been learned that multiple scattering is a source of additional data that contain retrievable information about cloud extinction and droplet size. In this paper we propose a retrieval method based on measurements at concentric multiple fields of view (MFOV) that applies these findings. The advantages are that there are no requirements for external boundary-value and backscatter-to-extinction data, and that solutions are obtained not only for the extinction coefficient but also for the droplet effective diameter d_e . From these primary solutions, quantities such as LWC and the extinction at other wavelengths can be derived with a minimum of approximations.

Multiple scattering in the MFOV lidar geometry is briefly discussed in Section 2, and the proposed retrieval algorithm is described in Section 3. In Section 4 we compare retrieval results of Monte Carlo simulated MFOV lidar returns with true values of extinction and droplet diameter. Finally, in Section

5 we discuss comparisons with in-cloud measurements recorded in a series of field experiments.

2. Multiple-Fields-of-View Lidar Method

Multiple scattering in lidar geometry is schematically depicted in Fig. 1. After entering a dense cloud, laser photons undergo several scatterings. In the single-scattering approximation, the scattered photons are considered lost. However, for particle sizes typical of cloud and precipitation droplets, a majority of the scattering events at visual and near-infrared wavelengths take place at small angles $\phi_i \lesssim 0.05$ rad, and the scattered photons remain within the field of view (FOV) θ of the receiver and are thus subject to detection. At narrow FOVs and medium ranges, most trajectories that contribute to the measured signal are made up of small-angle forward scatterings plus a single backscattering at an angle close to 180° . This is a basic hypothesis that we make throughout this paper. For this to be valid, the in-cloud diameter of the receiver footprint must be smaller than the scattering mean-free path equal to the inverse of the extinction coefficient. For an instrument dynamic range of $10^4 \approx \exp(9)$, and counting one scattering event per mean-free path, we can expect contributions up to a scattering order of ~ 9 . The number 9 here is the two-way optical depth at the detection limit of the system.

If the backscattering coefficient can be assumed uniform over the small range of backscattering angles close to 180° , Katsev *et al.*¹⁹ demonstrated that the physical cloud can be replaced for the purpose of calculations by a fictitious cloud of twice the extinction coefficient but with the same angular scattering properties in the forward direction and zero

where z is the range, θ is the receiver FOV, $P_{ss}(z)$ is the conventional single-scattering lidar equation, $M(z, \theta)$ is the multiple-scattering correction factor split into components F_d and F_g , respectively, for diffractive scattering alone and for all other scattering that involves at least one geometrical-optics scattering. The single-scattering equation is given by the well-known expression

$$P_{ss}(z) = \frac{K}{z^2} \beta(z) \exp[-2\tau(z)], \quad (2)$$

where K is a system or instrument constant, $\beta(z)$ is the backscatter coefficient, $\tau(z) = \int_0^z \alpha(z') dz'$ is the optical depth, and $\alpha(z)$ is the extinction coefficient.

The separation of M into F_d and F_g is done because the particle size information is contained primarily in the diffraction forward scattering. F_d and F_g are calculated by any suitable multiple-scattering model after we divide the angular scattering phase function $p(z, \phi)$ into diffraction and geometrical optics, i.e., reflection and refraction, components as follows:

$$p(z, \phi) = p_d(z, \phi) + p_g(z, \phi) + p_b(z, \phi), \quad (3)$$

where ϕ is the scattering angle, p_d is the diffractive component, p_g is the forward geometrical-optics component, and p_b accounts for all other scattering, mostly in the backward direction, not modeled by p_d and p_g . For polydisperse media, we suggest and use simple Gaussian models for p_d and p_g , i.e.,

$$p_d(z, \phi) = \frac{1}{2\omega} \frac{1}{\pi\theta_d^2(z)} \exp[-\phi^2/\theta_d^2(z)], \quad (4)$$

$$p_g(z, \phi) = A_4 \frac{(2\omega - 1)}{2\omega} \frac{1}{\pi\theta_g^2(z)} \exp[-\phi^2/\theta_g^2(z)], \quad (5)$$

where ω is the single-scattering albedo, θ_d and θ_g are the angular widths of the diffraction and geometrical-optics forward-scattering peaks, and $A_4 = 0.89$ is an empirical constant determined from best fits to a number of scattering phase function models for cloud droplets. A simple analytic expression for p_b is not known, and we must rely on Mie or more complex calculations where $p_b(z, \phi)$ is needed. The model described by Eqs. (3)–(5) is applicable for particle diameters larger than the wavelength. In accordance with Eq. (3), the extinction coefficient α is given by

$$\alpha(z) = \alpha_s(z) + \alpha_a(z), \quad (6)$$

with

$$\alpha_s(z) = \alpha_d(z) + \alpha_g(z) + \alpha_b(z), \quad (7)$$

where $\alpha_s = \omega\alpha$ is the scattering coefficient, α_a is the absorption coefficient, and $\alpha_d = \alpha_s/2\omega = \alpha/2$, $\alpha_g = \alpha_s A_4 (2\omega - 1)/2\omega = A_4 (2\omega - 1)\alpha/2$, and $\alpha_b = \alpha_s - \alpha_d - \alpha_g$ are the diffraction, the geometrical-optics, and the total backscatter components of the scattering coefficient, respectively.

Below we describe the solution steps to derive the

droplet effective diameter d_e and extinction coefficient α from the measured MFOV returns $P(z, \theta)$.

A. Initialization

We initialize the inversion procedure at a range z_{ms} , where multiple scattering becomes measurable with good precision. The measurable multiple-scattering threshold criterion is developed below. The requirements are that the single-scattering lidar equation (2) remains a valid approximation for all the ranges less than z_{ms} , and that asymptotic expressions can be derived to estimate the multiple-scattering functions F_d and F_g of Eq. (1) at z_{ms} .

To define the initialization conditions, we use the returns measured at the smallest and the largest fields of view, θ_{\min} and θ_{\max} , respectively. Let θ_{dd} and θ_{gg} be the characteristic angular widths of the functions $F_d(z, \theta)$ and $F_g(z, \theta)$. For cloud particles at visible and near-infrared wavelengths, $\theta_{dd} \ll \theta_{gg}$. Moreover, if θ_{\min} and θ_{\max} are chosen to satisfy the condition $\theta_{\min} \ll \theta_{dd} \ll \theta_{\max} \ll \theta_{gg}$, from Bissonnette *et al.*²⁴ we have

$$\tau(z) \approx \ln \left[1 + \frac{1}{\delta_d} \frac{P(z, \theta_{\max}) - P(z, \theta_{\min})}{P(z, \theta_{\min})} \right] \quad \text{for } z \leq z_{ms}, \quad (8)$$

where δ_d is the relative multiple-to-single-scattering backscatter coefficient, typically equal to 0.7 in water clouds at visible and near-infrared wavelengths. Approximation (8) with $\delta_d = 1$ can also be derived from Eloranta's analytical model²⁵ that was developed in the approximation of a Gaussian phase function. Approximation (8) means that the optical depth τ is calculable up to range z_{ms} from the system-independent relative strength of the MFOV returns. We used approximation (8) to determine the boundary value necessary to initialize the solution.

In practice, the conditions on θ_{\min} and θ_{\max} necessary to justify approximation (8) are often only marginally satisfied. Fortunately, the geometrical-optics contributions left out by assuming $\theta_{\max} \ll \theta_{gg}$ are nearly compensated by an overestimate of the diffraction scattering that results from the condition $\theta_{\max} \gg \theta_{dd}$. In practice this means that approximation (8) remains applicable over a wide enough range of optical depths as verified by Monte Carlo simulations.²⁴

To select a consistent z_{ms} , we first delimit a range interval where approximation (8) is valid. The criterion we use is that the ratio $P(z, \theta_{\max})/P(z, \theta_{\min})$ should be large enough to minimize experimental errors and yet small enough to justify the use of approximation (8) and of single-scattering solution methods at $z < z_{ms}$. For our system's θ_{\max} and θ_{\min} , experience has led us to choose the interval $[z_l, z_h]$ such that

$$1.2 \leq \frac{P(z, \theta_{\max})}{P(z, \theta_{\min})} \leq 1.5, \quad (9)$$

which is consistent with Monte Carlo simulations.²⁴

Next we calculate $\tau(z)$ in $[z_l, z_h]$ by substituting the measured returns for $P(z, \theta_{\max})$ and $P(z, \theta_{\min})$ in approximation (8). We then differentiate the resulting $\tau(z)$ to obtain the extinction coefficient $\alpha(z)$ in the interval $[z_l, z_h]$. Finally, we select within $[z_l, z_h]$ the range z_{ms} that is the closest to the maximum of $P(z, \theta_{\min})$. For the example depicted in Fig. 3, $z_{ms} \approx 460$ m. This z_{ms} is the range where the solutions are initialized.

The initialization procedure ends with calculation of the solution for the extinction coefficient α at all ranges of $z \leq z_{ms}$. To do this we use the Klett or backward integration method³ to invert the measured $P(z \leq z_{ms}, \theta_{\min})$ by solving the single-scattering lidar equation with the boundary value $\alpha(z_{ms})$ determined as outlined in the preceding paragraph. The validity of this solution rests on the approximations that $P(z, \theta_{\min}) \approx P_{ss}(z)$ and $\beta/\alpha \approx \text{constant}$ for $z \leq z_{ms}$. Since the optical depth $\tau(z_{ms})$ is relatively small, the errors on $\alpha(z \leq z_{ms})$ resulting from these approximations do not have a significant effect on the total optical depth over the complete lidar range.

B. Particle Diameter Retrieval Algorithm

The retrieval of particle size is based on the FOV dependence of the measured returns $P(z, \theta)$. In our lidar configuration of relatively short ranges and small FOVs, most of the θ dependence of $P(z, \theta)$ originates from the small-angle forward scattering that precedes and follows a single backscatter at an angle close to 180° as illustrated in the diagram of Fig. 1. These forward scatterings are heavily weighted by diffraction scatterings. The width θ_d of the diffractive forward peak, Eq. (4), of the scattering phase function of polydisperse droplets is inversely proportional to the effective droplet diameter d_e , or

$$\theta_d = 0.585(\lambda/d_e), \quad (10)$$

where d_e is the ratio of the third-order to the second-order moment of the droplet diameter distribution, λ is the lidar wavelength, and 0.585 is a fit parameter determined for modified gamma distribution functions. To retrieve d_e , we therefore need to relate θ_d to the field-of-view scale of the measured $P(z, \theta)$.

Although heavily weighted by diffraction, the field-of-view scale of $P(z, \theta)$ still depends in a nonnegligible fashion on refraction and reflection or geometrical-optics scattering. The first solution step, therefore, consists in extracting the diffraction contribution from the measured $P(z, \theta)$. According to Eq. (1), the diffraction contribution P_d is given by

$$\begin{aligned} P_d(z, \theta) &= P_{ss}(z)[1 + F_d(z, \theta)] \\ &= P(z, \theta) - P_{ss}(z)F_g(z, \theta), \end{aligned} \quad (11)$$

where P_{ss} and F_g are functions not directly measured that need to be determined. Deriving an expression for $P_{ss}(z)$ by fixing $\theta = \theta_{\max}$ in Eq. (1), we find that

$$\begin{aligned} P_d(z, \theta) &= P(z, \theta) - P(z, \theta_{\max})F_g(z, \theta)/[1 \\ &+ F_d(z, \theta_{\max}) + F_g(z, \theta_{\max})]. \end{aligned} \quad (12)$$

At this stage in the solution development, we want to evaluate P_d in the near field $z \leq z_{ms}$, where, according to the results in Subsection 3.A, we know the extinction coefficient $\alpha(z)$. Consequently, we can calculate $F_g(z, \theta)$ by running a direct-problem lidar simulation model since the geometrical-optics component $p_g(z, \phi)$ of the phase function is independent of θ_d as shown in Eq. (5) and that, for these small ranges of $z < z_{ms}$, there is little probability of a second-order diffraction scattering contributing to F_g . Then, there remains to specify $F_d(z, \theta_{\max})$. Since the condition $\theta_{\max} \gg \theta_{dd}$ is assumed to hold for $z \leq z_{ms}$, in the same approximation as that leading to approximation (8), we have

$$F_d(z, \theta_{\max}) \approx \delta_d \{ \exp[\tau(z)] - 1 \} \quad \text{for } z \leq z_{ms}, \quad (13)$$

which is independent of θ_d . Hence, for all the ranges of $z \leq z_{ms}$ we can extract the diffraction contribution $P_d(z, \theta)$ in terms of the measured $P(z, \theta)$, of the function F_g , calculable independently of θ_d , and of the approximation given by approximation (13).

For the direct-problem calculations of F_d , F_g , and M reported in this paper, we used the Bissonnette²⁶ model simplified by the equivalent-medium theorem of Katsev *et al.*¹⁹ This is not a requirement and other multiple-scattering models should work equally well.

To proceed, we need to determine a FOV scale, denoted θ_{md} , associated with $P_d(z, \theta)$. As for the scale θ_d of the diffraction peak of the scattering phase function, there is no absolute definition for θ_{md} . We describe θ_{md} as a scale that measures how fast or how slow $P_d(z, \theta)$ increases with the field of view θ . Since we do not have an analytical model of $P_d(z, \theta)$, we chose the following empirical expression for the purpose of deriving a value for θ_{md} :

$$P_d(z, \theta) = A + B\Phi(\theta^a/\theta_{md}^a), \quad (14)$$

where Φ is the error function, a is an exponent between 1 and 2, and A , B , and θ_{md} are parameters determined by a least-squares fit to the measured $P_d(z, \theta)$. The choice of Φ is arbitrary but it was selected for its simplicity and because it is a good representation of the θ dependence of $P_d(z, \theta)$. Exponent a is necessary because, in the limit of widespread uniform multiple scattering, $P_d(z, \theta)$ behaves asymptotically as θ^2 for small θ , whereas Φ is linear in its argument within the same limit. The simple model

$$a = 2 - 1/(1 + 0.3\tau) \quad (15)$$

gives satisfactory results in all the cases encountered thus far. Parameters A and B are not used in the retrieval, only the angular scale θ_{md} .

Next we need a model to write θ_d in terms of θ_{md} . Our objective is not to achieve a rigorous description but one that is robust even if limited in accuracy. In

Appendix A we propose a simple random walk model. The result is

$$\theta_d^2(z) = \frac{2}{b^2} \frac{\alpha(z)z}{\tau(z)} \theta_{md}^2(z) \left[1 + z \frac{d}{dz} \ln \theta_{md}(z) \right], \quad (16)$$

where b is a proportionality constant defined in Eq. (A1) and set equal to 0.65 for a best fit between the θ_{md} obtained from Eqs. (14) and (15) applied to Monte Carlo simulations and the assumed θ_d . The constant b is needed because, as discussed above, neither θ_d nor θ_{md} have absolute definitions; b allows us to put an equal sign in Eq. (16). Expressions other than Eqs. (4), (14), and (15) would have led to a different value of b , but the end result on d_e would be the same within the accuracy of the method. Finally, given θ_d , the required effective droplet diameter d_e is obtained by simple substitution in Eq. (10).

In principle, we can calculate θ_d from Eq. (16) by using the measured θ_{md} and the calculated solutions $\alpha(z)$ and $\tau(z)$. However, this requires differentiation of the experimental function $\ln \theta_{md}(z)$. The differentiation operation leads to large errors because the measured $\Delta\theta_{md}$ between range bins is of the order of the precision on θ_{md} . Although the actual $d \ln \theta_{md}/dz$ is small, especially far into the cloud, the resulting $z d \ln \theta_{md}/dz$ is easily of the order of unity and greater because z is generally large. Hence, evaluating $z d \ln \theta_{md}/dz$ solely on the basis of the measured θ_{md} was found impractical in the conditions encountered.

Here we propose a model to approximate $(1 + z d \ln \theta_{md}/dz)$. Since the derivative operates on $\ln \theta_{md}$, the result is a weak function of the absolute value of θ_{md} , which makes the development of a practical model more accessible. For example, close to the cloud base, we have, with reference to the diagram of Fig. 2, $\theta_{md} \sim \theta_d(z_b)(z - z_b)/z$. This gives $[1 + z d \ln \theta_{md}/dz] \sim z/(z - z_b)$, a purely geometric function. On the other hand, at large penetration depths we expect $z d \ln \theta_{md}/dz$ to tend to zero. We have calculated θ_{md} for several Monte Carlo simulations and found from the results that an acceptable model is

$$\begin{aligned} & \left[1 + z \frac{d}{dz} \ln \theta_{md}(z) \right] \\ & \approx \begin{cases} 0.15 \left(\frac{z_1 + z}{z - z_b} \right) - 3.4 & \text{if greater than } 1 + z_2/z, \\ 1 + z_2/z & \text{otherwise} \end{cases}, \end{aligned} \quad (17)$$

with

$$z_1 = 28/\alpha(z), \quad (18)$$

$$z_2 = z_1(\overline{\theta_d}/35)^2, \quad (19)$$

where z , z_b , z_1 , z_2 , and α must be expressed in consistent units, and where θ_d , expressed in milliradians, is θ_d averaged over $[z_b, z]$. Although the model is a function of θ_d through the second branch of approximation (17), $[1 + z d \ln \theta_{md}/dz]$ can still be evaluated

explicitly because, for $z < z_{ms}$, it is the first branch that applies and, for $z > z_{ms}$, the solution $\theta_d(z)$ is known at all ranges smaller than z .

The model of approximation (17) is, of course, not rigorous and subject to future improvements as a greater variety of conditions is encountered. Should particular experimental conditions allow the evaluation of $d \ln \theta_{md}/dz$ with acceptable precision from the measured data, that would definitely be the preferred option.

C. Extinction Retrieval Algorithm

Here we describe the retrieval of the extinction coefficient $\alpha(z)$ for $z > z_{ms}$. The proposed algorithm requires first the determination of the system constant K that appears in Eq. (2). The calculation of K is performed at the initialization range z_{ms} . At this stage in the inversion process we know the solutions $\alpha(z)$ and $d_e(z)$ for $z \leq z_{ms}$, missing are the multiple-scattering function $M(z_{ms}, \theta)$ and the backscatter coefficient $\beta(z_{ms})$. Making use of the solution $d_e(z \leq z_{ms})$, assuming knowledge of the type and shape of the particles, and fitting a general function for size distribution, e.g., a modified gamma function for water clouds, one can calculate the corresponding phase function and backscatter-to-extinction ratio $\beta(z)/\alpha(z)$. With these results and the solution $\alpha(z \leq z_{ms})$, it is then possible to evaluate $M(z_{ms}, \theta)$ for the applicable geometry by use of any suitable direct-problem simulation model of multiply scattered lidar returns. The relative errors on the retrieved $d_e(z \leq z_{ms})$, which become important as multiple scattering decreases with decreasing z , do not have a serious effect because the absolute multiple-scattering contributions become vanishingly small in that region. Finally, it is a simple matter to calculate K by substituting the measured $P(z_{ms}, \theta)$ and the derived solution $\alpha(z_{ms})$, $\tau(z_{ms})$, $\beta(z_{ms})$, and $M(z_{ms}, \theta)$ in Eqs. (1) and (2). It is worth mentioning that a new constant is obtained for each set of MFOV returns. Therefore the calibration errors are completely independent from one MFOV set to another.

Having determined the value of K , we can now proceed to ranges $z > z_{ms}$. The extinction and droplet size solutions are run simultaneously and the nonlinear coupling between α , β , d_e , τ , F_d , and F_g is handled by iterations at each range step.

After incrementing the range to z , the values of $\alpha(z)$ and $\tau(z)$ are extrapolated from the solutions at the preceding step. Then we sequentially calculate the droplet size $d_e(z)$, the backscatter-to-extinction ratio $k(z) = \beta/\alpha$, and the multiple-scattering functions $F_d(z, \theta)$, $F_g(z, \theta)$ and $M(z, \theta)$ using the last updated $d_e(z)$ and $\alpha(z)$ and the solutions already derived for all the ranges less than z . These calculations are performed by use of the size retrieval algorithm of Eqs. (10), (16), (18), and (19) and approximation (17), and suitable phase function and multiple-scattering calculation codes. Finally, the extinction coefficient is updated by substitution of all

these quantities in the multiple-scattering lidar equation, or more precisely, in the expression

$$\alpha(z) = \frac{1}{K} \frac{z^2}{k(z)} \exp[2\tau(z)] \times \frac{M(z, \theta_{\min})^s P^{1+s}(z, \theta_{\max})}{M(z, \theta_{\max})^{1+s} P^s(z, \theta_{\min})}. \quad (20)$$

Equation (20) is actually the solution for the back-scattering coefficient $\beta(z)$ transformed into the extinction coefficient $\alpha(z)$ through the calculated ratio $k(z)$. This is done because it is through the back-scattering coefficient that the lidar returns depend most on local cloud properties. The solution is written in terms of the ratio $P^{1+s}(z, \theta_{\max})/P^s(z, \theta_{\min})$ instead of $P(z, \theta)$ because, formulated in this fashion, the multiple-scattering terms in Eq. (20) counterbalance more effectively the exponential function $\exp(2\tau)$ that can cause serious instabilities. Exponent s is actually chosen to factor out the explicit occurrence of $\exp(2\tau)$ in Eq. (20). More precisely, we require

$$\frac{M^{1+s}(z, \theta_{\max})}{M^s(z, \theta_{\min})} = \exp(2\tau). \quad (21)$$

Solving for s , we find

$$s(z) = \frac{2\tau(z) - \ln M(z, \theta_{\max})}{\ln M(z, \theta_{\max}) - \ln M(z, \theta_{\min})}. \quad (22)$$

After $\alpha(z)$ is obtained from Eq. (20), we go back to the solution for $d_e(z)$ and iterate all the calculations until the new $d_e(z)$ and $\alpha(z)$ differ from the preceding ones by less than the preset margins. After convergence is attained, we proceed to the next range bin and restart the iterations. We terminate the solutions when $P(z, \theta_{\min})$ reaches the instrument noise level.

If the multiple-scattering model for M and the solutions at all ranges preceding z were exact, the proportionality relation

$$\frac{P(z, \theta_{\max})}{P(z, \theta_{\min})} = \frac{M(z, \theta_{\max})}{M(z, \theta_{\min})} \quad (23)$$

would hold true for all z and the value of exponent s would have no effect whatsoever on the calculation of $\alpha(z)$. In practice

$$\frac{P(z, \theta_{\max})}{P(z, \theta_{\min})} \frac{M(z, \theta_{\min})}{M(z, \theta_{\max})} \neq 1, \quad (24)$$

and experience has shown that the value of s derived from Eq. (22) helps to stabilize the solution process and, as a result, to maintain the ratio of inequality (24) close to unity.

The solutions obtained from Eq. (20) are in most cases quite satisfactory but there are cases in which the calculated $\alpha(z)$ drifts with increasing range. To solve this problem and obtain consistent solutions, we refine the solutions with a final iteration process after

recasting the multiple-scattering lidar equation as follows:

$$S(z) = \frac{1}{K} \frac{P(z, \theta)}{M(z, \theta)} \frac{z^2}{k(z)} = \alpha(z) \exp[-2\tau(z)]. \quad (25)$$

Equation (25) has exactly the same form as the single-scattering lidar equation and, therefore, has the following solution given by the backward-integration Klett method³:

$$\alpha(z) = \frac{S(z)}{S(z_f)/\alpha_f + 2 \int_z^{z_f} S(z') dz'}, \quad (26)$$

where z_f is the far range of the lidar return and α_f is the boundary value at z_f . For α_f we choose the $\alpha(z)$ derived at the preceding iteration step and averaged over the last few range bins, and for z_f we choose the range at which $P(z, \theta_{\max})$ drops to the noise level. This definition of the far range gives a z_f greater than the maximum range for the solution defined by Eq. (20) since we obtained the latter by applying the noise threshold to $P(z, \theta_{\min})$. It is obvious in Fig. 3 that z_f can be greater by tens of meters. This extra range gives additional room for the convergence of Eq. (26) to a solution independent of the error on α_f . Finally, for $M(z, \theta)$ and $k(z)$ that enter the definition of $S(z)$, we use the functions already computed. Note that the calibration constant K is factored out of Eq. (26).

With the new $\alpha(z)$ and $\tau(z)$, we rerun the algorithm for the computation of the effective droplet diameter $d_e(z)$, which allows us to obtain new estimates of $M(z, \theta)$ and $k(z)$. We can then go back to Eq. (26) and start a new iteration. We repeat these iterations until proper convergence is obtained, which generally requires two to three cycles.

The results of the whole process are the range-resolved solutions for the effective droplet diameter and extinction coefficient over the complete lidar range defined by a valid signal in the smallest field of view. Calculations for a typical cloud penetration depth of 200 m at a resolution of 3 m takes 2–5 s on a Pentium II processor.

4. Monte Carlo Simulations

We carried out a first validation study by inverting Monte Carlo simulations of MFOV lidar returns. The Monte Carlo code²⁷ was developed with the least possible set of hypotheses. The scattering probabilities were derived from the exact phase function and not from the simplified model of Eqs. (3)–(5) on which the inversion is based. The required phase functions were calculated for spherical water droplets and both log-normal and modified gamma distributions were used. We performed the phase function computations with the Mie code given by Bohren and Huffman.²⁸ For the cases studied here, we have not included depolarization. Finally, we have applied only well-established variance reduction techniques, namely, the analytic computation at each photon in-

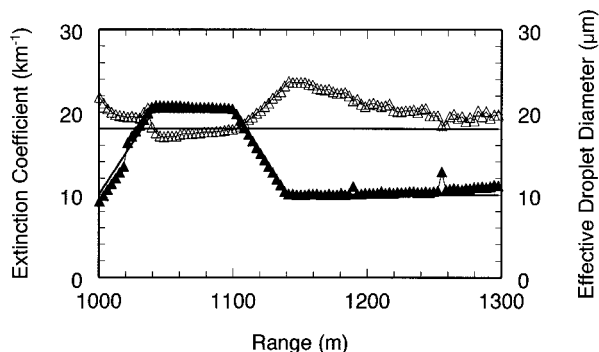


Fig. 4. Comparison of true and retrieved extinction coefficients and effective droplet diameters for Monte Carlo simulated lidar returns from a vertically stratified cloud at 1000 m. Continuous curves for true values and symbols for retrievals: filled for extinction and open for droplet diameter.

teraction of the probability of backscatter into the receiver (e.g., Brusciaglioni *et al.*²⁹), and the symmetrization of the phase function.³⁰ We tested the code by comparing results with those of the thoroughly validated code of Brusciaglioni *et al.*²⁹ for exactly the same inputs and number of scattering orders. Exact agreement was found. In summary, the code provides simulated MFOV lidar returns without simplifying assumptions on the phase function and propagation geometry and in a manner totally independent of the modelization used to derive the inversion method of Section 3.

The simulations were carried out to an optical depth of ~ 4 by use of eight scattering orders, 10^9 photons, and a range bin size of 3 m. The laser pulse was assumed coaxial with the receiver telescope and of infinitesimal length. The computed signals are in units of $W/J \text{ m}^2$, i.e., per joule of laser pulse energy and square meters of receiver aperture area.

The validation procedure consisted in running several simulation cases, inverting the results to retrieve the extinction coefficient $\alpha(z)$ and effective droplet diameter $d_e(z)$ with the same range resolution as used in the Monte Carlo calculations, and comparing the retrieved and true values. A specific example of a comparison between the retrieved and the true $\alpha(z)$ and $d_e(z)$ profiles is illustrated in Fig. 4 for a vertically stratified cloud of optical depth 4.2 located 1000 m from the lidar. We found excellent agreement for the extinction coefficient except at the top of the cloud at which the extinction is overestimated by $\sim 10\%$ as a result of the convergence lag in the solution of Eq. (26). Other methods of evaluating the boundary value α_f can give better results in specific cases but we found that the method described in Subsection 3.C is preferable for the ensemble of cases studied thus far. The droplet size is at some ranges overestimated by as much as 25% but, most importantly, we observed that the solution recovers quite well from local perturbations. We consider that a precision of 20–30% for the droplet diameter is quite satisfactory considering the large number of crude simplifications that were necessary to derive the FOV

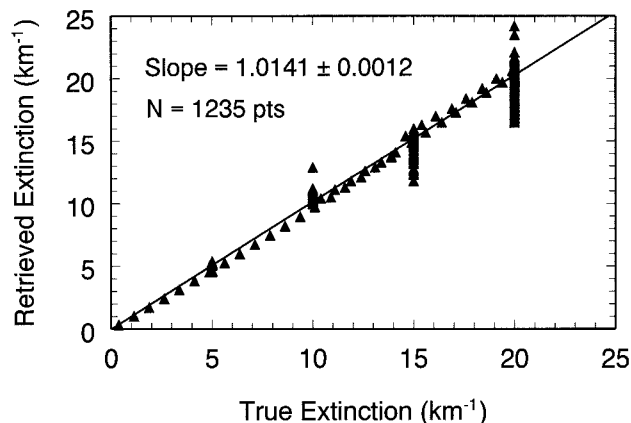


Fig. 5. Retrieved versus true extinction coefficients for a series of Monte Carlo simulated returns from clouds of various extinction coefficients, droplet sizes, profiles, and ranges to cloud base. Retrievals and true values are sampled at a range resolution of 3 m. The straight line represents the least-squares fit to the data points.

scale $\theta_{md}(z)$ and, through Eqs. (16), (18), and (19) and approximation (17), the width $\theta_d(z)$ of the local phase function diffraction peak. The precision and consistency of the droplet diameter solutions deteriorate near the base of the cloud at which the amount of multiple-scattering contributions becomes marginal for a reliable evaluation of θ_{md} .

The comparisons for all the runs are summarized in the form of scatterplots for the extinction coefficient and effective droplet diameter in Figs. 5 and 6, respectively. All the data for all the range values are reported. The simulations included inhomogeneous clouds as depicted in Fig. 4, and homogeneous clouds of constant extinction coefficient and effective droplet diameter.

In Fig. 5 the straight line constrained to pass through the origin is the least-squares fit through the data points. The values of the calculated slope and the standard deviation are quoted on the graph. The agreement is better than 2% on average. However, there are extreme points at which the retrieved extinction is in error by $\sim 25\%$ but, because the standard deviation of the slope is small as indicated in Fig. 3, the number of such cases is small. In other words, most of the points fall close to the fitted line.

The droplet size results of Fig. 6 reveal a good correlation up to an effective diameter of $\sim 20 \mu\text{m}$. The diameters at small scattering strength, namely, for $P(z, \theta_{\max})/P(z, \theta_{\min}) < 1.05$, have been screened out of Fig. 6 because the calculation of d_e becomes unreliable with the decrease in multiple-scattering contribution as discussed above. The plotted solid line is the identity line shown for reference. The least-squares fitted slope for all the diameters less than $20 \mu\text{m}$ is 1.035 ± 0.003 . Hence, for these droplets, the retrieval method is in error by less than 4% on average. The maximum deviation, if we remove the four outliers at $16 \mu\text{m}$, is 25%, which is quite acceptable given the precision of the model of Eqs. (16), (18), and (19) and approximation (17).

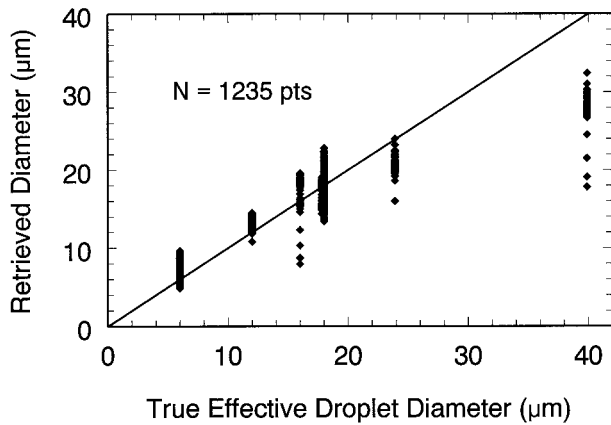


Fig. 6. Retrieved versus true effective droplet diameters for a series of Monte Carlo simulated returns from clouds of various extinction coefficients, droplet sizes, profiles, and ranges to cloud base. Retrievals and true values are sampled at a range resolution of 3 m. The straight line represents the identity line that was drawn for reference.

The droplet sizes greater than 20 μm are underestimated by an amount that increases with droplet size. This comes from the geometry of detection. Indeed, the large droplets scatter radiation in a forward cone of ever-decreasing angular width with increasing size to the point at which a large fraction of the multiply scattered photons are recorded within the smallest FOV of the instrument as can be visualized from the diagram of Fig. 1 or Fig. 2. Under such conditions, the FOV scale θ_{md} of the multiple-scattering contributions cannot be determined with accuracy. For a given range, the amount of hidden multiple scattering grows with droplet size and the error on θ_{md} increases in agreement with the results of Fig. 6. The limit depends on the smallest FOV and the distance to cloud base. The smallest FOV is constrained by the laser beam divergence. In the present simulations, we used $\theta_{\min} = 0.5$ mrad and a distance to the cloud base of $z_b = 500$ m, which corresponds to our lidar smallest FOV and to an overlap range that guarantees minimal FOV cross talk over a cloud of reasonable depth. Therefore, the retrieval errors beyond 20 μm are not a limit of the solution method but a limit imposed by the application geometry, particularly the distance z_b to cloud base with regard to the scattering mean-free path and the system's technical specifications.

The simulations at 16 μm were actually carried out for a bimodal particle size distribution made up of 98.5% of droplets of an effective diameter of 16 μm and 1.5% of 60- μm droplets. It is clear, following the discussion of the preceding paragraph, that the 60- μm droplets are beyond size resolution for the assumed system and application parameters. It is therefore a positive result on the consistency of the retrieval method that it yielded values close to only 16 μm .

One important characteristic of an inversion method is stability to measurement noise. It is

therefore essential to add noise to the Monte Carlo simulations. Monte Carlo calculations have inherent variance but, here, the natural Monte Carlo fluctuations were kept small by use of variance reduction and 10^9 trajectories. To evaluate the noise contributions in physically meaningful terms, we considered the experimental situation that corresponds to our current mode of operation. In short, the principal source of error arises from the sequential measurement of the different FOV returns. The laser is pulsed at 100 Hz and the FOV is changed at the same rate. Thus returns at different FOVs are recorded from separate laser pulses spaced by as much as 1/3 s since there are 32 FOVs. Hence, the combined effects of pulse-to-pulse fluctuations in laser output energy and temporal changes in the probed can introduce important relative variations in $P(z, \theta)$.

The operation mode generally consists in firing bursts of 1000 lidar shots (10-s duration) that contain 1000/32 complete sets of MFOV returns. From these, we construct an average $\langle P(z, \theta) \rangle$ from 20 sets since we omit the leading seconds of the burst to allow good laser thermalization. It is this average return that is generally used for retrieval. To quantify the errors that are due to nonsimultaneous recordings, we calculated the standard deviation of the relative difference $[P(z, \theta) - \langle P(z, \theta) \rangle] / \langle P(z, \theta) \rangle$ over all the returns that were used to calculate $\langle P(z, \theta) \rangle$. In the worst case, the observed error on $P(z, \theta)$ is less than 20%. Since we averaged $P(z, \theta)$ over 20 consecutive MFOV sets, i.e., over 6.1 s, the residual standard deviation measurement error for $\langle P(z, \theta) \rangle$ was reduced by a factor of $\sqrt{20}$ to $\sim 4.5\%$.

In addition, the signal has random detector noise. For the simulations we assumed a noise level of 1.5×10^{-5} W/J m^2 , which corresponds to a signal-to-noise ratio of 10^4 at the base of a 20- km^{-1} cloud located at 1000 m. As in the preceding case, the additive noise level was also reduced by summation to $\sim 3.4 \times 10^{-6}$ W/J m^2 .

The random noise that results from the nonsimultaneous measurement of the FOVs was applied between FOVs only, not between ranges, since the return for a given θ is from a single laser pulse and lasts only a few microseconds. However, the electronic noise was added independently to each (z, θ) pair. The noisy returns $P(z, \theta)$ were thus calculated as follows:

$$P(z, \theta) = P_{mc}(z, \theta)[1 + \sigma_{ns}f_1(\theta)] + \text{NEP}f_2(z, \theta), \quad (27)$$

where P_{mc} is the noise-free Monte Carlo simulation, σ_{ns} is the summation-reduced pulse-to-pulse standard deviation of the relative lidar return chosen equal to 0.045 as discussed above, i.e., the worst case, NEP is the noise-equivalent power set equal to 3.4×10^{-6} W/J m^2 , $f_1(\theta)$ is a Gaussian random variable of unit standard deviation parameterized in θ , and $f_2(z, \theta)$ is a different random variable also of unit standard deviation parameterized in both z and θ . We as-

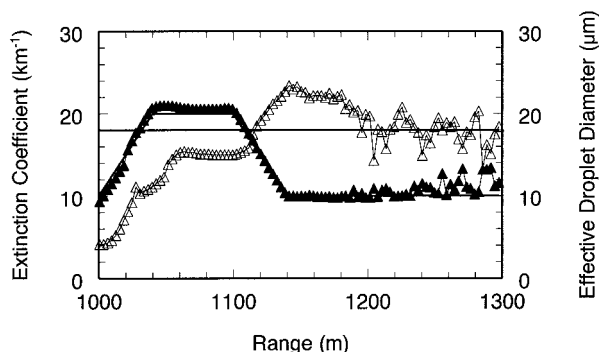


Fig. 7. Same as Fig. 2 except that the Monte Carlo simulations were noise corrupted as described by Eq. (27) with $\sigma_n = 0.045$ and a NEP of 3.4×10^{-6} W/J m².

sume complete statistical independence between f_1 and f_2 .

The calculated solutions for the corrupted $P(z, \theta)$ for the same example as in Fig. 4 are shown in Fig. 7. We observed little degradation of the extinction solution except for some fast fluctuations at the far end where the additive noise becomes significant. For the droplet diameter, in addition to the oscillations at the far range, there is underestimation at the base of the cloud where the multiple-scattering contributions are small compared with $\sigma_{ns}P_{mc}$. Even for this worst-case situation, the differences with the uncorrupted case remain in general within the 20–25% margin that constitutes the limit for d_e as discussed earlier in this section. The larger systematic differences at very small optical depths are not unexpected because the information-bearing multiple scattering becomes of the order of or smaller than $\sigma_{ns}P_{mc}$ and thus highly distorted. Instruments that would record all FOVs simultaneously would remedy this situation. Finally, it should be noted that the solution recovers well from this initial error.

5. Comparisons with Field Data

A. Experiment

We recently participated in the Alliance Icing Research Study (AIRS) experiment that took place at Mirabel, Québec, in the winter of 1999–2000. The main objectives of the experiment were the characterization of cloud and precipitation conditions leading to in-flight icing of aircraft, and the testing of potential remote sensors of icing hazards. The general preliminary results are summarized by Isaac *et al.*^{31,32} The AIRS experiment was well suited for validation of the lidar retrieval method. The lidar was located on the airport grounds within a few hundred meters from the main runway. The instrumented aircraft flew various flight patterns consisting of horizontal level passes at different altitudes above the runways, spirals centered on the lidar, and missed approaches. In other words, the cloud layer at the site was thoroughly probed vertically and horizontally for periods of 1–3 h at a time.

B. Lidar Measurements

The fielded MFOV lidar is a Nd:YAG system with the following specifications: 1.06- μ m wavelength, 70-mJ pulse energy, 12-ns pulse duration, 25-mm beam diameter at the transceiver, 0.5-mrad beam divergence, selectable pulse repetition frequency up to 100 Hz, 200-mm-diameter telescope receiver colinear with the laser axis, and variable fields of view (FOVs). We changed the FOVs at the chosen laser repetition frequency of 100 Hz by rotating a 125-mm-diameter aluminized glass disk with apertures of different sizes etched at equidistant angular intervals. The disk was positioned in the image plane of the main telescope mirror. The laser Q switch was slaved to the disk rotation velocity to ensure that the FOV apertures were in position on the lidar axis in synchronization with the laser pulses. The disk has 32 apertures defining 32 FOVs between 0.1 and 12-mrad full angle. A complete FOV scan takes 32/100 s, during which time it is assumed that the cloud remains unchanged. The FOV footprints on a cloud at 1 km are, respectively, 1 and 12 m in diameter for the smallest and largest FOVs of 1 and 12 mrad that were used for the retrieval.

After passage through the FOV aperture, the collected radiation was collimated, separated into parallel and perpendicular polarization components, and focused on 3-mm-diameter Si avalanche photodiodes used in the analog mode. The detector outputs were fed to 4.5-decade logarithmic amplifiers. The log amplifier outputs were digitized at 100, 50, or 25 MHz, depending on cloud height, for range bin sizes of 1.5, 3, or 6 m, respectively. The range resolution defined by the pulse length is 1.8 m.

The lidar was operated in two modes. When air traffic control would allow, the lidar beam was elevation scanned in a vertical plane parallel to the main runway. In this mode, we were able to map the spatial and temporal variations of the lidar backscatter and depolarization. This has produced unique data on the structure and phase of clouds and precipitation. These results are discussed in Bissonette *et al.*³³ and Roy *et al.*³⁴ Because our sequential method of changing the FOVs is incompatible with a rapidly moving lidar axis, we performed MFOV measurements in a stare mode only. To penetrate deeper into the cloud layer, we chose vertical pointing. The stare mode operation consisted in firing bursts of 1000 pulses at the laser repetition rate of 100 Hz, every minute for periods of 1–3 h. For each burst, we therefore have $1000 \div 32 = 31$ complete sets of MFOV returns. The MFOV retrieval method requires only one of those sets, which corresponds to a 1/3-s snapshot of the cloud. To minimize fluctuation errors, we generally averaged over 6 s or 18 consecutive MFOV sets. We decided on 6 s because we discarded the first seconds of the bursts to allow for sufficient thermalization of the laser. Halving the averaging time produced little difference in the retrieved values; in other words, the 6-s averaging time is not a critical parameter.

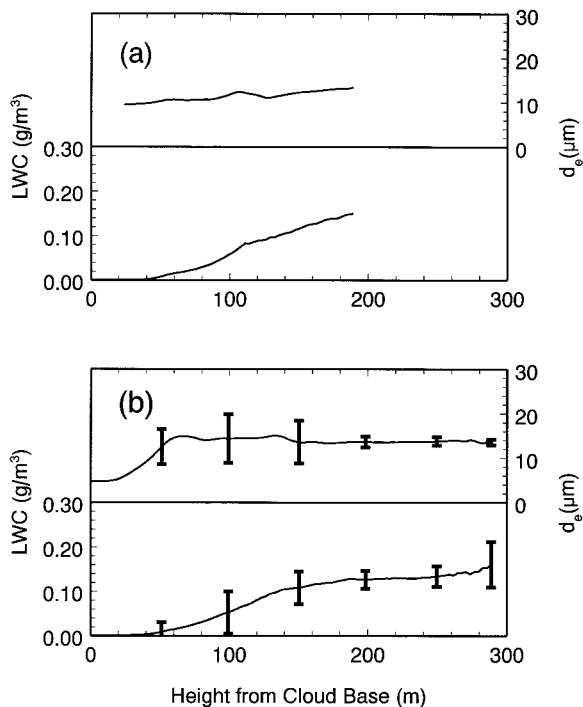


Fig. 8. Example of lidar solutions for LWC and effective droplet diameter d_e as functions of height from the base of a stratus cloud deck: (a) instantaneous solutions at 21:00 UTC on 3 December 1999 and (b) averaged solutions over a 1-h period, i.e., 20:50–21:50 UTC on 3 December 1999. The vertical bars indicate \pm one standard deviation of temporal fluctuations. The height resolution is 3 m.

The primary solution results for each burst are the profiles of the extinction coefficient $\alpha(h)$ and the effective droplet size $d_e(h)$, where h is the height above ground. The relevant cloud microphysical parameters measured by the aircraft that we can compare with lidar retrievals are the LWC and the droplet diameter. Assuming that the extinction efficiency is equal to 2 for the cloud droplets contributing most to α and the LWC and noting that the effective diameter is defined as the ratio of the third-order to the second-order moments of the size distribution, the LWC can be readily calculated from $\alpha(h)$ and $d_e(h)$ as follows:

$$\text{LWC}(h) = \frac{1}{3} \rho \alpha(h) d_e(h), \quad (28)$$

where ρ is the density of liquid water. An example of the retrieved solutions for one MFOV burst is shown in Fig. 8(a). The profiles are plotted as functions of height measured from cloud base determined for each burst from the raw lidar signals. For the case of Fig. 8(a) the lidar-derived cloud base was at 1020 m above ground level. The prevailing conditions were rather stable, the cloud base varied by less than 100 m over the preceding hour. The temperature measured 35 min earlier was 2.4 °C at the 1000-m level. The solutions plotted in Fig. 8(a) show a lidar penetration depth in the bulk of the cloud of ~ 150 m. The maximum LWC is of the order of 0.15 g/m³ and the ef-

fective droplet diameter reached 13.5 μm . The droplet diameter solution begins at ~ 30 m; below that level, the multiple-scattering contributions are too small for a reliable solution.

The retrieved individual solutions fluctuate from burst to burst, i.e., from 1 min to the next even though the cloud layer may appear stable. Figure 8(b) shows the same LWC and d_e solutions but averaged over 1 h; the error bars indicate the \pm one standard deviation of the fluctuations observed over that period. The averages are calculated over same-height sets of LWC data referenced to the local and instantaneous cloud base. The resulting average profiles have a greater penetration depth than the instantaneous profile of Fig. 8(a) because there are times within the 1-h period when the cloud density is less in the cloud base region. The error bars indicate that the temporal fluctuations were typically $\pm 35\%$ for both LWC and d_e in the bulk of the cloud. As will be seen, the greatest part of these fluctuations match and are even smaller than the natural fluctuations observed by the aircraft *in situ* sensors and are therefore real and not measurement or retrieval errors.

C. In Situ Measurements

The Canadian National Research Council Convair-580 aircraft was employed during the AIRS. The aircraft was instrumented by the Cloud Physics Research Division of the Meteorological Service of Canada, and the complete set of onboard cloud microphysical sensors is described by Isaac *et al.*³¹ Instruments used for the investigation reported here (see Cober *et al.*³⁵) included a Particle Measuring System, Inc. (PMS) King probe LWC meter, a Sky Tech Research, Inc. Nevzorov liquid and total water content meter, two PMS forward-scattering spectrometer probes (FSSPs) and three PMS two-dimensional (2-D) probes. The calibration and quality control of measurements taken with these instruments have been described by Cober *et al.*³⁵ The King and Nevzorov probes are used to measure LWC within 15%. The FSSP instruments are used to measure collectively droplet sizes and concentrations between 3 and 95 μm in diameter, whereas the three 2-D probes are used to measure collectively hydrometeor shapes, sizes, and concentrations from approximately 100 to 6000 μm in diameter. The aircraft data were averaged over 30-s periods corresponding to a horizontal length of approximately 3 km. For each 30-s period, the FSSP and 2-D measurements were combined to determine the entire drop spectra from 3 to 3000 μm . For each drop spectrum, the effective diameter and LWC could be computed with 15% and 40% accuracy, respectively. Similarly, the 2-D probes were used to determine the ice crystal spectra from 100 to 6000 μm . The cloud phase of each 30-s period was determined as liquid, mixed, or glaciated following the methodology outlined by Cober *et al.*^{35,36}

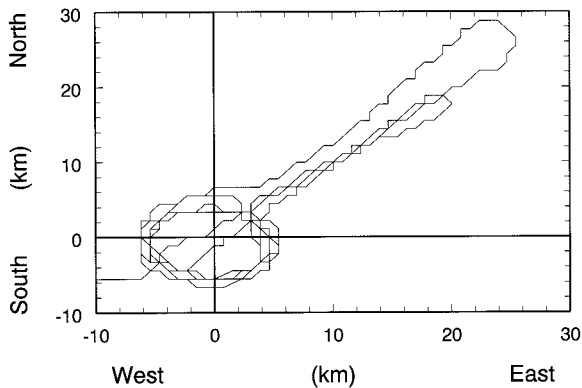


Fig. 9. Horizontal projection of a typical aircraft track for 20:50–21:50 UTC on 3 December 1999. The lidar position is at (0,0).

D. Comparison Results

It is obvious that the comparisons between the aircraft and the lidar data cannot be done on a point-by-point basis. The lidar spatial resolution is a cube of typically 2 m on the sides, whereas each aircraft sensor sweeps a sampling volume of the order of 1 cm wide by ~50 m long for the highest temporal resolution of 1 s. In addition, the aircraft flies in the general airport area covering tens of kilometers, whereas the lidar probes the cloud in a fixed vertical column. Consequently, the quantitative comparisons are done on statistical parameters only. The statistics were constructed from data collected during the same time periods. Figure 9 is one example of a horizontal flight track over a 1-h period. The map of Fig. 9 is centered on the lidar position. As can be seen, the aircraft circled or spiraled within a radius of ~5 km from the lidar position, flew level passes along the southwest–northeast direction of the main runway to distances as far as 40 km from the lidar, and completed two missed approaches.

Despite the obvious differences between the lidar and the aircraft data sets, we can still expect a fair degree of statistical similarity. Indeed, for the conditions of stratus cloud decks experienced during the AIRS, it appears justifiable to postulate statistical horizontal homogeneity over scales of a few tens of kilometers and statistical stationarity over periods of 1–2 h. If we make this assumption, we can compare the statistics of parameters measured at different positions and times within the acceptable homogeneous and stationary domains. In other words, it seems reasonable to assume that the 1-h-plus sets of lidar measurements recorded at one position are statistically comparable with sets of aircraft data collected over a horizontal expanse of a few tens of kilometers within the general area of the lidar position and during the same period. One characteristic of the experiment that further supports this assumption is that the aircraft flew, as shown in Fig. 9, a pattern aligned with the main airport runway which, by definition, parallels the direction of prevailing winds.

The cloud parameters we chose to compare were the LWC and the effective droplet diameter d_e . The

measurements by the aircraft hot-wire probes and size spectrometers and by the lidar are all affected, but to a different degree, by the presence of ice crystals. It is therefore important to eliminate from the comparisons the data that contain a significant amount of ice crystals. The aircraft data used for the comparisons were screened to include only liquid- and mixed-phase cloud conditions with ice crystal concentrations less than 1/liter. In these cases, the liquid-water fraction was always greater than 85% of the total hydrometeor water content, and the PMS FSSP and 2-D instrument measurements of drop sizes and concentrations were not significantly affected by the presence of ice crystals (Cober *et al.*³⁵). For the lidar, we required that the linear depolarization at the smallest FOV, for minimal multiple-scattering contamination, be smaller than 0.1, which ensures a net predominance of spherical droplets on the backscatter lidar return. The depolarization threshold is set relatively high because of unavoidable depolarization by multiple scattering and because, at small signal strength, logarithmic amplifier inaccuracies tend to increase artificially the measured depolarization ratio by a few percent.

The LWC was determined from the King and the Nevzorov LWC probes and averaged at 30-s resolution. The effective diameter and drop spectrum LWC were determined from the combined FSSP and 2-D probe data at 30-s resolution. To ensure that we retained only in-cloud data for our comparisons, we discarded all the measurements with $LWC < 0.02$ g/m³. In the case of lidar, since we had the height of the cloud base for each measurement, we additionally removed the points that were less than 50 m from the cloud base. We further degraded the height resolution of the remaining solution points to 20 m for statistical decorrelation between the sampled values. For each measurement event or flight number Table 1 lists the date, the overlap period, and the populations of the validated liquid-phase data sets for the lidar and the aircraft King, Nevzorov, and size spectrometer sensors. One record was deleted from the size spectrometer set of 7 December because the corresponding effective droplet diameter constituted a definite outlier.

The LWC averages and standard deviations calculated over the duration of the events are plotted in Fig. 10 as functions of the event or flight number. There is reasonable correlation between the lidar and the other sensors; the highs and the lows coincide. However, there are two distinct regions; for the first three events, the lidar-derived average LWC and its standard deviation are much lower than for the aircraft sensors, whereas they appear comparable and show good correlation for the last four events. Similar results for the effective droplet diameter are shown in Fig. 11. In this case, the agreement is much closer for both the average value and the standard deviation, and the correlation between the two data sets is good.

Can the results of Fig. 10 be explained by lidar retrieval errors? To investigate this, we have sin-

Table 1. Validated Liquid-Phase Data Sets^a

| Flight No | Date | Overlap Period UTC | Population of Data Set | | | |
|-----------|------------------|-----------------------|------------------------|------|----------|---------------|
| | | | Lidar | King | Nevzorov | Spectrometers |
| 100 | 2 December 1999 | 19:20–21:50 | 797 | 96 | 96 | 98 |
| 101 | 3 December 1999 | 20:50–21:50 | 385 | 62 | 60 | 60 |
| 102 | 6 December 1999 | 18:50–20:30 | 384 | 114 | 114 | 113 |
| 103 | 7 December 1999 | 14:00–15:00 | 175 | 5 | 5 | 4 |
| 108 | 15 December 1999 | 16:40–18:30 | 397 | 46 | 46 | 45 |
| 109 | 16 December 1999 | 18:50–21:30 | 312 | 41 | 45 | 40 |
| 113 | 28 January 2000 | 18:20–19:45 | 79 | 5 | 5 | 5 |

^aData derived from the lidar and the aircraft King probe, Nevzorov probe, and size spectrometers for the full cloud layer.

gled out flight 102 as a case study. Among the set of events studied here, it is the instance of largest average LWC encountered by the aircraft. We propose to determine whether the lidar could have penetrated the layer defined by the aircraft LWC sensors and thus verify the compatibility between the lidar and the aircraft data sets.

First, in Fig. 12 we compare the lidar and the King probe LWC profiles of flight 102. The King probe profile was derived from the aircraft 1-s data. The aircraft altitude is referenced to the average cloud base height for the period, i.e., 540 m, whereas the lidar data are, referenced to the base value determined for each lidar burst. Figure 12 shows the event-averaged curves and the instantaneous data,

actually only a sample of the complete sets to avoid overcrowding an already busy graph. The aircraft instantaneous data are actually averaged over 30 s or over a 25% change in altitude measured from the cloud base, whichever comes first. It can be seen that both the lidar and the aircraft profiles have the same general shape but the constant level reached by the lidar solution is almost three times as small as that measured by the King probe.

Next, from the results of Fig. 12 we calculated the column-integrated water $CIW_k(h)$ for the King probe by integrating over the average profile as follows:

$$CIW_k(h) = \int_0^h \langle LWC_k(h') \rangle dh', \quad (29)$$

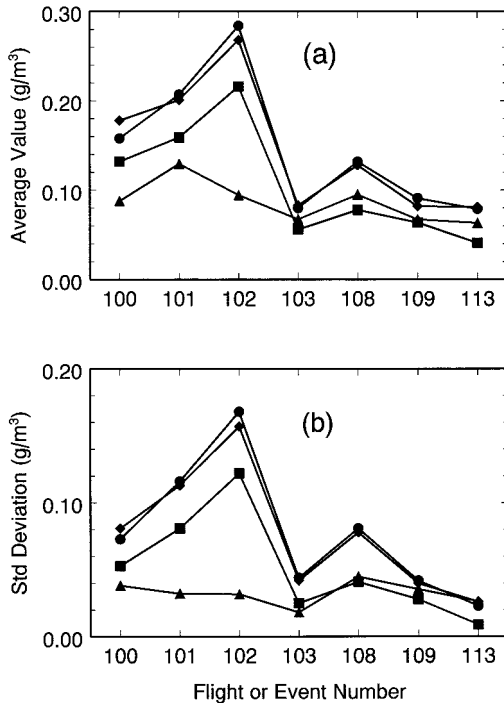


Fig. 10. LWC average properties as functions of flight number. The flight numbers, dates, and overlap periods over which averages were calculated are listed in Table 1. *In situ* data are from the complete layer probed by aircraft: filled triangles, lidar; filled circles, King probe; filled diamonds, Nevzorov probe; filled squares, size spectrometer; (a) average value and (b) standard deviation.

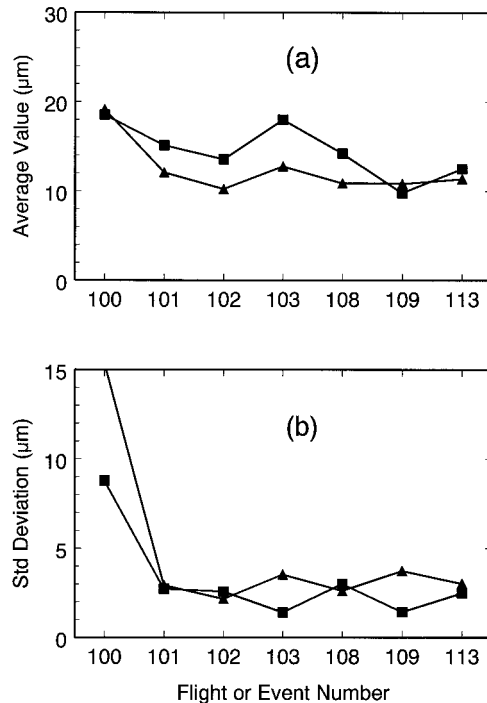


Fig. 11. Effective droplet diameter average properties as functions of flight number. The flight numbers, dates, and overlap periods over which averages were calculated are listed in Table 1. *In situ* data are from the complete layer probed by aircraft: filled triangles, lidar; filled squares, size spectrometer; (a) average value and (b) standard deviation.

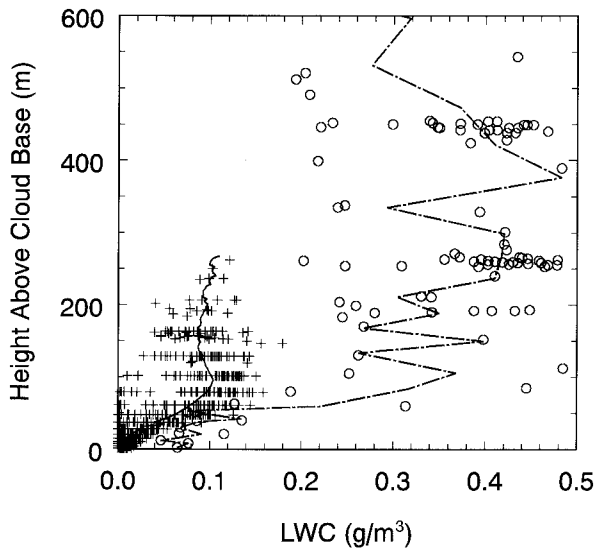


Fig. 12. Average and instantaneous LWC profiles for 18:50–20:30 on 6 December 1999, flight 102: continuous curve, average lidar profile; dot–dash curve, average King probe profile; pluses, instantaneous lidar solutions; open circles, instantaneous King probe measurements.

where $\langle \text{LWC}_k \rangle$ is the average King probe profile, h is the height above the cloud base, and the integral limit 0 refers to the cloud base. The cloud base was stable during flight 102 and equal to 540 m. Using Eq. (28) to relate the LWC to the extinction coefficient at the lidar wavelength and assuming a constant effective droplet diameter $d_e = 13.5 \mu\text{m}$ given by the size spectrometer average value in Fig. 11 for flight 102, we found that the optical depth $\text{OD}_k(h)$ traversed by the lidar pulse to height h derived from the aircraft King probe data is

$$\text{OD}_k(h) = \frac{3}{\rho d_e} \text{CIW}_k(h) = 0.22 \text{CIW}_k(h), \quad (30)$$

where the $\text{CIW}_k(h)$ is expressed in grams per square meter.

Finally, in Fig. 13 we compare $\text{OD}_k(h)$ with the $\text{OD}_l(h)$ obtained by integration of the average lidar solution for the extinction coefficient. Also shown in Fig. 13 is the relative number of lidar instantaneous values that contribute at each height h to the average $\text{OD}_l(h)$. As expected from Fig. 12, the optical depth profiles of Fig. 13 differ considerably. For example, at the penetration depth of 160 m reached by 80% of all the recorded lidar pulses, the lidar solutions give an optical depth of 3.7 compared with 8 for the King probe. In the single-scattering approximation, the lidar signal is attenuated by a factor $\exp(-2 \times \text{OD})$. Multiple scattering contributes to lowering the attenuation. At the smallest FOV of 1-mrad (full angle) used to determine the penetration depth, the multiple-scattering enhancement factor at 160 m calculated by Monte Carlo runs is less than 2 for the cloud defined by the lidar solutions and less than 20 for the cloud defined by the King probe and size spectrometer measurements. The resulting attenuation

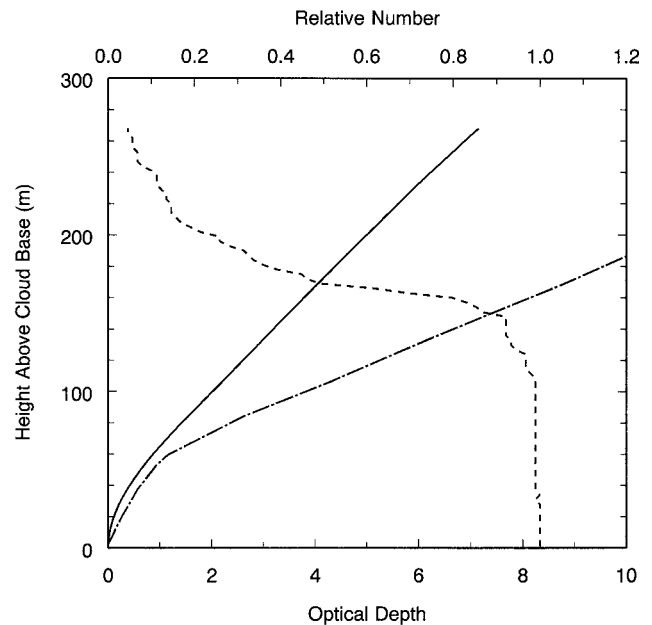


Fig. 13. Average optical depth profile for 18:50–20:30 on 6 December 1999: solid curve, calculated from the average lidar solution for extinction coefficients; dot–dash curve, calculated from the King probe average profile of Fig. 12 according to Eqs. (29) and (30); dashed curve (top axis), relative number of instantaneous lidar solution points that contribute, at each height, to the calculated average profile.

of $2 \exp(-2 \times 3.7) \approx 1.2 \times 10^{-3}$ is compatible with the dynamic range of 3×10^4 of the lidar but certainly not $20 \exp(-2 \times 8) \approx 2.3 \times 10^{-6}$. The 160-m penetration depth was calculated from time of flight in both measurements and Monte Carlo simulations.

The penetration depth is one quantity that is completely independent of the retrieval method, which one can simply determine by recording the time of flight at which the collected signal drops to the noise level. Therefore, on the basis of the results of Fig. 13, we can state with confidence that the lidar pulses could not have physically penetrated the cloud characterized by the aircraft King probe and size spectrometer data to the depths actually observed, regardless of the lidar retrieval method. In other words, the large extinction values derived from flight 102 measurements are incompatible with the lidar observations. Hence, the solution method of this paper is not invalidated by the results of flight 102. Incidentally, all the lidar solutions for all the events are consistent with the lidar dynamic range. We have no ready explanation for these discrepancies; they could result from the inadequacy of the assumed statistical equivalence between the aircraft and the lidar samplings, from the presence of large droplets, or from some yet unidentified causes. Large droplets would have been missed by the lidar as discussed in Section 4, but the aircraft sensors that have a range extending to millimeter-size particles did not record large droplets. Hence, the large droplet hypothesis appears unlikely.

For comparison of Figs. 10 and 11, we used the

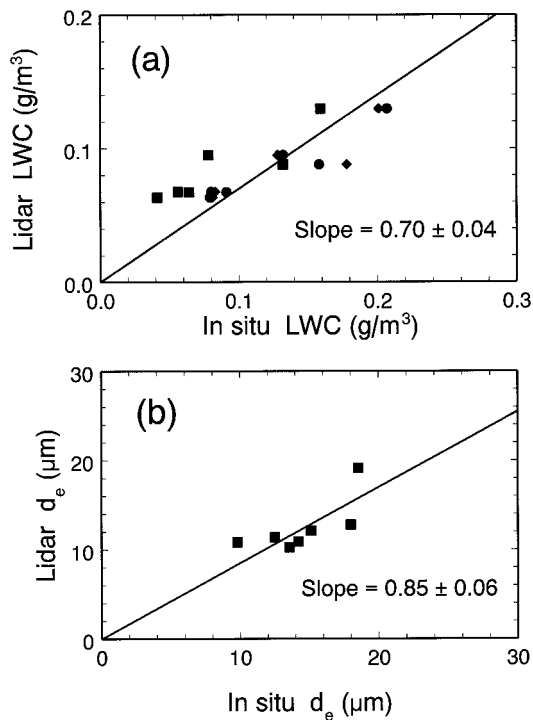


Fig. 14. Scatterplot of lidar-derived versus full-layer (a) *in situ* measurements of LWC and (b) effective droplet diameter. The plotted values are the data of Figs. 10(a) and 11(a). Filled circles, King probe; filled diamonds, Nevzorov probe; filled squares, size spectrometer.

aircraft data from all the altitudes regardless of the limited cloud depths probed by the lidar. To verify whether there could be an altitude bias, we have rerun the comparison of Figs. 10 and 11 with the subsets of aircraft data comprised between 50 and 300 m from the cloud base. The resulting differences are not statistically significant although the size of some of the aircraft data subsets is marginal. A notable exception is flight 102 in which the average aircraft LWC for the cloud base region is 25% greater than for the full layer, actually in the wrong direction to explain a possible altitude bias caused by the lidar retrieval method.

To quantify the general level of agreement, in Fig. 14 we reproduced the data of Figs. 10 and 11 in the form of scatterplots of the lidar LWC and d_e solutions versus the aircraft sensor measurements. We have excluded from the LWC scatterplot the results of flight 102 because, as just discussed, the large differences cannot be attributed to errors in the lidar solutions. We have kept the results of flights 100 and 101 because the differences could, within the limit, be accounted for by measurement and solution errors, but for those two events there remains a good probability of bias of similar origin as in flight 102. The effective droplet diameter is less dependent on where the samples come from in the cloud deck, and, for this reason, the droplet size data of flight 102 were not removed from the analysis. The plots of Fig. 14 confirm the relatively good correlation as well as the

Table 2. Least-Squares Fitted Proportionality Constants^a

| Data Set | Average Value | |
|---------------|-----------------|-----------------|
| | LWC | d_e |
| All | 0.70 ± 0.04 | — |
| King | 0.66 ± 0.04 | — |
| Nevzorov | 0.65 ± 0.05 | — |
| Spectrometers | 0.87 ± 0.10 | 0.85 ± 0.06 |

^aBetween lidar retrievals and aircraft *in situ* sensor measurements for the average value of LWC and d_e .

biases between the lidar and the *in situ* measurements. Table 2 lists the slope values or the proportionality constants for the various data sets. According to these results, the lidar solutions underestimate the LWC and the droplet diameter by 30% and 15%, respectively. Both values are within the quoted limits of 40% and 15% for the LWC and d_e derived from the size spectrometers, but 30% is greater than the expected 15% accuracy of the King and Nevzorov LWC probes. Actually, the difference between the lidar and the hot-wire probes is of the same order as between the spectrometers and the hot-wire probes that, incidentally, share the same platform and are thus unaffected by vastly different sampling methods. In summary, the lidar retrievals agree with the *in situ* measurements to within a 35% bias at worst. In the case of the large 35% bias with the hot-wire probes, we have seen that it cannot be attributed solely to lidar solution errors.

6. Conclusion

We have described in detail a lidar remote sensing retrieval method based on the measurement of multiple-scattering contributions to the collected lidar returns. The solution main products are the range-resolved extinction coefficient and effective particle diameter. The solutions do not require the specification of a boundary value and a backscatter-to-extinction ratio from independent information or measurements. This and the simultaneous retrieval of the effective particle diameter constitute two significant advantages over conventional solution methods for dense media. As a result, the solutions are self-contained and can be extended to secondary products such as the liquid-water content of liquid-phase clouds and the extinction coefficients at wavelengths other than the lidar's.

The validation tests with Monte Carlo simulations are particularly significant because the true values are known exactly. The results show biases and statistical errors for both the extinction coefficient and the effective particle diameter of less than 5%. They also illustrate clearly the limitations of the method. The first limitation has to do with the strength of multiple scattering. Since the boundary value is replaced by the relative strength of multiple scattering, the experimental conditions must be such that multiple scattering is measurable with sufficient accuracy. For the method to work, we determined that

the return at the system's largest field of view must be 20–30% larger than the single-scattering level. The second limitation has to do with particle size. The algorithm is based on resolving at the receiver position the diffraction forward peak of the angular scattering function. Given the beam divergence, the angular resolution of the telescope–detector assembly and the distance to the scattering medium, there is a predictable limit on the resolvable FOV width of $P(z, \theta)$ as can be visualized in the diagram of Fig. 1 or Fig. 2. Since the width of the forward diffraction peak is inversely proportional to particle size, the method therefore cannot discriminate particles greater than a calculable size. For the Monte Carlo simulations in this paper with ranges to a cloud base greater than 500 m, the limit was found to be $\sim 20 \mu\text{m}$ as illustrated in Fig. 6. Conversely, if the particles are too small, the diffraction peak is either too wide for the angular range of the receiver or difficult to distinguish from the geometrical-optics scatterings that are virtually independent of size. For the 1.06- μm lidar system used to record the data reported here, the lower limit is $\sim 3 \mu\text{m}$.

The method was also tested in the field against *in situ* measurements inside low-altitude liquid-phase clouds. Seven case studies of clear liquid-phase clouds were examined. The comparisons are not absolute because the *in situ* samples never coincided spatially with the lidar probings; separation distances constantly varied and ranged from 5 to 40 km horizontally. Since the periods of simultaneous measurements lasted 1–2 h, we have assumed statistical equivalence between the two data sets and the comparisons were carried out on average and standard deviation values. The results of these comparisons indicate that there is at worst a 35% bias between the lidar and the *in situ* sensor measurements of LWC and 15% on effective droplet size. We have shown that the bias cannot be attributed solely to the lidar method. For at least one event, the recorded lidar penetration depth was clearly greater than the dynamic range-limited depths predicted on the basis of the aircraft data. There is good indication that a similar situation, although less evident, exists for two other events, namely, flights 100 and 101. By comparison, all lidar extinction solutions, which are calculated without reference to the instrument dynamic range, turned out to be consistent with that range. Typically, our lidar cannot measure returns beyond an optical depth of ~ 4 .

The solutions yield with acceptable consistency the LWC and effective droplet diameter of liquid-phase clouds, two parameters of primary concern to assess cloud effects on climate. Interestingly, the field results show that the retrieved solutions remain statistically representative of the complete layer, with a bias of at most 35%, despite the limited penetration range. Although we still need to look at more varied liquid-phase cloud conditions than encountered during the AIRS experiment, particularly for LWC, this observation certainly lessens the often raised objection of limited lidar sounding depth. Long-term

MFOV lidar monitoring could thus become a practical and economical option for cloud statistical studies. The addition of a microwave radiometer could provide the needed estimate of the full layer thickness by combining average LWC and integrated water column.

In conclusion, the proposed MFOV lidar method is well validated by the combined Monte Carlo and field tests reported in this paper. The solutions are sufficiently well correlated with true values and measurements to justify the search for a more rigorous basis of many of the proposed multiple-scattering-based solution steps, especially for droplet size.

Appendix A: Model of the Angular Spread of Multiply Diffraction-Scattered Lidar Returns

The object of the proposed model is to relate θ_d , the width of the forward diffraction peak of the scattering phase function, to θ_{md} , the measured FOV scale of the diffraction contribution to the multiply scattered lidar return, i.e., P_d of Eq. (11). Our goal is not to derive a rigorous model but one that is robust even if limited in accuracy. We formulate θ_{md} within the framework of the equivalent-medium theorem of Katssev *et al.*¹⁹ This theorem allows substitution of the true scattering medium by a fictitious medium that has twice the extinction coefficient in the forward direction of the lidar path but zero extinction in the return leg as depicted in Figs. 1 and 2. Making use of this simplified geometry, we equate the angle θ_{md} to the angle subtended at the transceiver by the average lateral distance $\sqrt{\langle \rho^2 \rangle}$ at which a photon has migrated from the lidar axis after having undergone only forward diffraction scatterings. More specifically, we set

$$\theta_{md} = b \frac{\sqrt{\langle \rho^2 \rangle}}{z}, \quad (\text{A1})$$

which is valid in the paraxial approximation, where b is a proportionality constant to be determined *a posteriori* and where $\langle \dots \rangle$ denotes ensemble averaging.

Referring to Fig. 15 for a schematic representation of the forward scatterings and a definition of the variables, we have

$$\langle \rho^2(z) \rangle = \left\langle \left\{ \int_{z_0}^z \xi(z') \cos \phi(z') dz' \right\}^2 \right\rangle + \left\langle \left\{ \int_{z_0}^z \xi(z') \sin \phi(z') dz' \right\}^2 \right\rangle, \quad (\text{A2})$$

where z_0 is the range to cloud base, and ξ and ϕ are the direction angles of the scattered ray. Invoking statistical independence between ξ and ϕ and assuming local homogeneity, i.e.,

$$\langle \xi(z_1) \xi(z_2) \rangle \approx \langle \xi^2(z_1) \rangle f_{\xi}(z_1 - z_2), \quad (\text{A3})$$

$$\langle \cos \phi(z_1) \cos \phi(z_2) \rangle \approx \langle \cos^2 \phi(z_1) \rangle f_{\phi}(z_1 - z_2), \quad (\text{A4})$$

$$\langle \sin \phi(z_1) \sin \phi(z_2) \rangle \approx \langle \sin^2 \phi(z_1) \rangle f_{\phi}(z_1 - z_2), \quad (\text{A5})$$

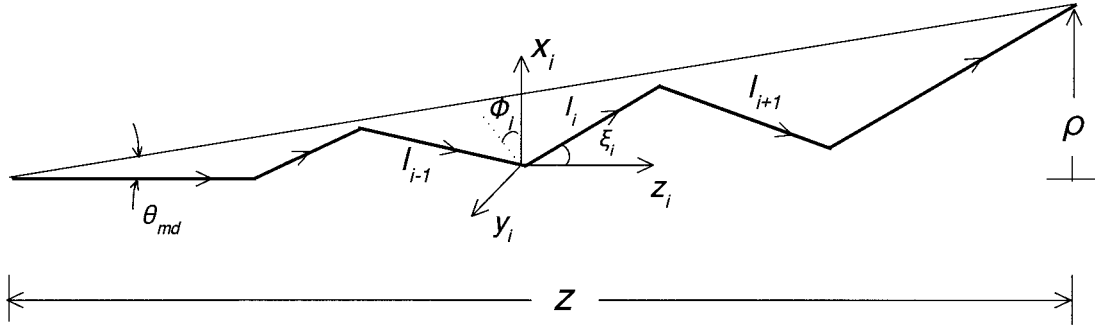


Fig. 15. Schematic representation of the forward-scattering events that contribute to the average angle θ_{md} subtended at the transceiver by the diffraction-scattered photons.

from Eq. (A2) we obtain the following simplified expression for $\langle \rho^2(z) \rangle$:

$$\langle \rho^2(z) \rangle = \int_{z_0}^z dz_1 \langle \xi^2(z_1) \rangle \int_{z_1-z}^{z_1-z_0} du f_{\xi}(u) f_{\phi}(u). \quad (\text{A6})$$

The integral over the correlation function $f_{\xi} f_{\phi}$ defines a characteristic length

$$l(z_1) = \int_{z_1-z}^{z_1-z_0} du f_{\xi}(u) f_{\phi}(u). \quad (\text{A7})$$

From Eqs. (A1), (A6), and (A7), for θ_{md} we find

$$\theta_{md}^2(z) = \frac{b^2}{z^2} \int_{z_0}^z dz_1 \langle \xi^2(z_1) \rangle l(z_1). \quad (\text{A8})$$

Finally, differentiating Eq. (A8) with respect to z , we obtain

$$\langle \xi^2(z) \rangle = \frac{2}{b^2} \frac{z \theta_{md}^2(z)}{l(z)} \left[1 + z \frac{d}{dz} \ln \theta_{md}(z) \right]. \quad (\text{A9})$$

Since $\langle \xi^2(z) \rangle$ is the variance of the scattering angle after N scattering convolutions, we have, assuming Gaussian statistics,

$$\langle \xi^2(z) \rangle \simeq N(z) \theta_d^2(z), \quad (\text{A10})$$

where $N(z)$ is the number of diffraction scattering events encountered by a photon up to range z . The θ_d of Eq. (A10) is not, strictly speaking, a local property. Equation (A10) is a simplification that loses its accuracy if the droplet size distribution changes rapidly with z . In practice, the droplet effective diameter remains rather constant over the relatively short cloud penetration depths at visible and near-infrared lidar wavelengths and the smoothing that results from approximation (A10) is acceptable. We approximate $N(z)$ as follows:

$$N(z) = \tau(z) / \{1 - \exp[-\tau(z)]\}, \quad (\text{A11})$$

which tends to 1 in the limit $\tau \rightarrow 0$ and is equal to τ for $\tau \gg 1$, as expected. Note that the asymptotic number of scatterings is equal to τ and not 2τ , the total round-trip optical depth, because diffraction

contributes only one-half of the total extinction for particles large compared with the wavelength as assumed here. In addition, we model

$$l(z) = \{1 - \exp[-\tau(z)]\} / \alpha(z). \quad (\text{A12})$$

Within the limit of vanishing τ , $l(z) \sim (z - z_0)$ in accordance with its definition and, for large τ , $l(z)$ becomes equal to the scattering mean-free path $1/\alpha(z)$. Combining Eqs. (A9), (A11), and (A12) and approximation (A10), we obtain the required expression that links θ_d to the measured FOV scale θ_{md} , i.e.,

$$\theta_d^2(z) = \frac{2}{b^2} \frac{\alpha(z) z}{\tau(z)} \theta_{md}^2(z) \left[1 + z \frac{d}{dz} \ln \theta_{md}(z) \right]. \quad (\text{A13})$$

We are grateful for the able technical assistance of Gilles Vallée and Sylvain Cantin. We also thank the organizers of the AIRS for inviting us despite the troublesome laser eye-safety issue and the authorities and personnel of Air Traffic Control at Montreal Mirabel Airport for their constant cooperation. The Meteorological Service of Canada of Environment Canada, the Institute for Aerospace Research of the National Research Council of Canada, the National Search and Rescue Secretariat of Canada, the Canada Department of National Defence, Boeing Commercial Airplane Group, Transport Canada, NASA Glenn, and the FAA provided funding for the data collected during the AIRS.

References

1. K. Sassen, G. G. Mace, Z. Wang, M. R. Poellet, S. M. Sekelsky, and R. E. McIntosh, "Continental stratus clouds: a case study of coordinated remote sensing and aircraft measurements," *J. Atmos. Sci.* **56**, 2345–2358 (1999).
2. K. Sassen, "The polarization lidar technique: a review and current assessment," *Bull. Am. Meteorol. Soc.* **72**, 1848–1866 (1991).
3. J. D. Klett, "Stable analytical inversion solutions for processing lidar returns," *Appl. Opt.* **20**, 211–220 (1981).
4. F. G. Fernald, "Analysis of atmospheric lidar observations: some comments," *Appl. Opt.* **23**, 652–653 (1984).
5. L. R. Bissonnette, "Sensitivity analysis of lidar inversion algorithms," *Appl. Opt.* **25**, 2122–2125 (1986).
6. C. M. R. Platt and T. Takashima, "Retrieval of water cloud

- properties from carbon dioxide lidar soundings," *Appl. Opt.* **26**, 1257–1263 (1987).
7. S. A. Young, "Analysis of lidar backscatter profiles in optically thin clouds," *Appl. Opt.* **34**, 7019–7031 (1995).
 8. S. T. Shipley, D. H. Tracy, E. W. Eloranta, J. T. Trauger, J. T. Stroga, F. L. Roesler, and J. A. Weinman, "High spectral resolution lidar to measure optical scattering properties of atmospheric aerosols. 1. Theory and instrumentation," *Appl. Opt.* **22**, 3716–3724 (1983).
 9. J. T. Stroga, E. W. Eloranta, S. T. Shipley, F. L. Roesler, and P. J. Tryon, "High spectral resolution lidar to measure optical scattering properties of atmospheric aerosols. 2. Calibration and data analysis," *Appl. Opt.* **22**, 3725–3732 (1983).
 10. A. Ansmann, M. Riebesell, and C. Weitkamp, "Measurement of atmospheric aerosol extinction profiles with a Raman lidar," *Opt. Lett.* **15**, 746–748 (1990).
 11. J. D. Spinhirne, J. A. Reagan, and B. M. Herman, "Vertical distribution of aerosol extinction cross section and inference of aerosol imaginary index in the troposphere by lidar technique," *J. Appl. Meteorol.* **19**, 426–438 (1980).
 12. Y. Sasano and H. Nakane, "Quantitative analysis of RHI lidar data by an iterative adjustment of the boundary condition term in the lidar solution," *Appl. Opt.* **26**, 615–616 (1987).
 13. D. Gutkowitz-Krusin, "Multiangle lidar performance in the presence of horizontal inhomogeneities in atmospheric extinction and scattering," *Appl. Opt.* **32**, 3266–3272 (1993).
 14. G. J. Kunz and G. de Leeuw, "Inversion of lidar signals with the slope method," *Appl. Opt.* **32**, 3249–3256 (1993).
 15. G. Roy, G. Vallée, and M. Jean, "Lidar-inversion technique based on total integrated backscatter calibrated curves," *Appl. Opt.* **32**, 6754–6763 (1993).
 16. S. Elouragini, "Useful algorithms to derive the optical properties of clouds from a backscatter lidar return," *J. Mod. Opt.* **42**, 1439–1446 (1995).
 17. R. J. Allen and C. M. R. Platt, "Lidar for multiple backscattering and depolarization observations," *Appl. Opt.* **16**, 3193–3199 (1977).
 18. C. Flesia and P. Schwendimann, eds., Topical feature on *Multiple-Scattering Lidar Experiments*, *Appl. Phys. B* **60**, 315–362 (1995).
 19. I. L. Katsev, E. P. Zege, A. S. Prikhach, and I. N. Polonsky, "Efficient technique to determine backscattered light power for various atmospheric and oceanic sounding and imaging systems," *J. Opt. Soc. Am. A* **14**, 1338–1346 (1997).
 20. L. R. Bissonnette and D. L. Hutt, "Multiple scattering lidar," *Appl. Opt.* **29**, 5045–5046 (1990).
 21. D. L. Hutt, L. R. Bissonnette, and L. Durand, "Multiple field of view lidar returns from atmospheric aerosols," *Appl. Opt.* **33**, 2338–2348 (1994).
 22. L. R. Bissonnette and D. L. Hutt, "Multiply scattered aerosol lidar returns: inversion method and comparison with *in situ* measurements," *Appl. Opt.* **34**, 6959–6975 (1995).
 23. G. Roy, L. R. Bissonnette, C. Bastille, and G. Vallée, "Retrieval of droplet-size density distribution from multiple-field-of-view cross-polarized lidar signals," *Appl. Opt.* **38**, 5202–5211 (1999).
 24. L. R. Bissonnette, G. Roy, L. Poutier, S. G. Cober, and G. A. Isaac, "Lidar remote sensing of cloud liquid water content and effective droplet diameter: retrieval method and comparison with Monte Carlo simulations and *in situ* measurements," TR 2002-20 (Defence Research and Development Canada Establishment Valcartier, 2459 Pie XI Blvd. North, Val-Bélair, Québec G3J 1X5, Canada), to be published.
 25. E. W. Eloranta, "Practical model for the calculation of multiply scattered lidar returns," *Appl. Opt.* **37**, 2464–2472 (1998).
 26. L. R. Bissonnette, "Multiple-scattering lidar equation," *Appl. Opt.* **35**, 6449–6465 (1996).
 27. L. Poutier, "Evaluation de la technique de sondage par lidar à champs de vue multiples," Technical Report No. RTS 2/05101 DOTA (ONERA, Office National d'Etudes et Recherches Aéronautiques, Centre de Toulouse, 2 ave Edouard Belin, 31055 Toulouse, France, 2001).
 28. C. F. Bohren and D. R. Huffman, *Absorption and Scattering of Light by Small Particles* (Wiley, New York, 1983), Appendix A.
 29. P. Brusciaglioni, A. Ismaelli, and G. Zaccanti, "Monte-Carlo calculations of lidar returns: procedure and results," *Appl. Phys. B* **60**, 325–329 (1995).
 30. C. M. R. Platt, "Remote sensing of high clouds III: Monte Carlo calculations of multiple-scattered lidar returns," *J. Atmos. Sci.* **38**, 156–167 (1981).
 31. G. A. Isaac, S. G. Cober, J. W. Strapp, A. V. Korolev, A. Tremblay, and D. L. Marcotte, "Recent Canadian research on aircraft in-flight icing," *Can. Aeronaut. Space J.* **47**(3), 213–221 (2001).
 32. G. A. Isaac, S. G. Cober, J. W. Strapp, D. Hudak, T. P. Ratvasky, D. L. Marcotte, and F. Fabry, "Preliminary results from the Alliance Icing Research Study (AIRS)," paper AIAA-2001-0393, presented at the 39th Aerospace Science Meeting and Exhibit, Reno Nevada, 8–11 January 2001, (American Institute of Aeronautics and Astronautics, Reston, Va., 2001).
 33. L. R. Bissonnette, G. Roy, and F. Fabry, "Range-height scans of lidar depolarization for characterizing properties and phase of clouds and precipitation," *J. Atmos. Oceanic Technol.* **18**, 1429–1446 (2001).
 34. G. Roy and L. R. Bissonnette, "Strong dependence of rain-induced lidar depolarization on the illumination angle: experimental evidence and geometrical-optics interpretation," *Appl. Opt.* **40**, 4770–4789 (2001).
 35. S. G. Cober, G. A. Isaac, A. V. Korolev, and J. W. Strapp, "Assessing cloud phase conditions," *J. Appl. Meteorol.* **40**, 1967–1983 (2001).
 36. S. G. Cober, G. A. Isaac, and A. V. Korolev, "Assessing the Rosemount icing detector with *in-situ* measurements," *J. Atmos. Oceanic Technol.* **18**, 515–528 (2001).